

## Appendix

### 1. Experimental Methods

#### 1.1 The X-ray Analysis Cell

The X-ray analysis cell incorporated the following features:

1. **Temperature Control:** We introduced a heater and a thermocouple into the “clamp plate” and “transparent resin plate” (as depicted in Figure S1.1) to maintain uniform temperatures across critical regions such as the cathode flow channel, anode flow channel, and membrane electrode assembly (MEA).
2. **Torque Management:** By tightening the four “M4×40 screws” (shown in Figure S1.1) using a torque driver, we ensured consistent operating conditions without risking damage to the carbon flow path plate. This approach minimized gas and liquid leaks.
3. **Carbon flow path plate:** Flow plates made of carbon were adopted to mitigate the undesired X-ray adsorption losses. Collimated X-rays were directed parallel (in-plane) to the carbon flow channels. It is estimated that a 15 keV X-ray beam would be attenuated to 60.1% after passing through both edges of the carbon flow plate (a total of 4 mm in width).
4. **Transparent Resin Plate:** We modified the flow path design by allowing the protrusions on the “transparent resin plate” to partially penetrate the “carbon flow path plate.” This design enables visual observation of the flow path within the X-ray analysis cell.
5. **Camera Mounting:** We attached a fixture (shown in Figure S1.2) that holds a CMOS camera directed toward the “transparent resin plate” for the through-plane visible-light observation of the cathode channels.

The MEA consisted of an anode, a cathode, and a membrane. The anode was an IrO<sub>x</sub>/Ti porous electrode (De Nora Permelec), and the membrane was an anion exchange membrane (AEM; PiperION, Versogen). The cathode was a carbon paper with a micro-porous layer (Sigracet 28BC, SGL Carbon), which was spray-coated with an Au/C catalyst (20% Au on Vulcan XC-72, Fuel Cell Store).

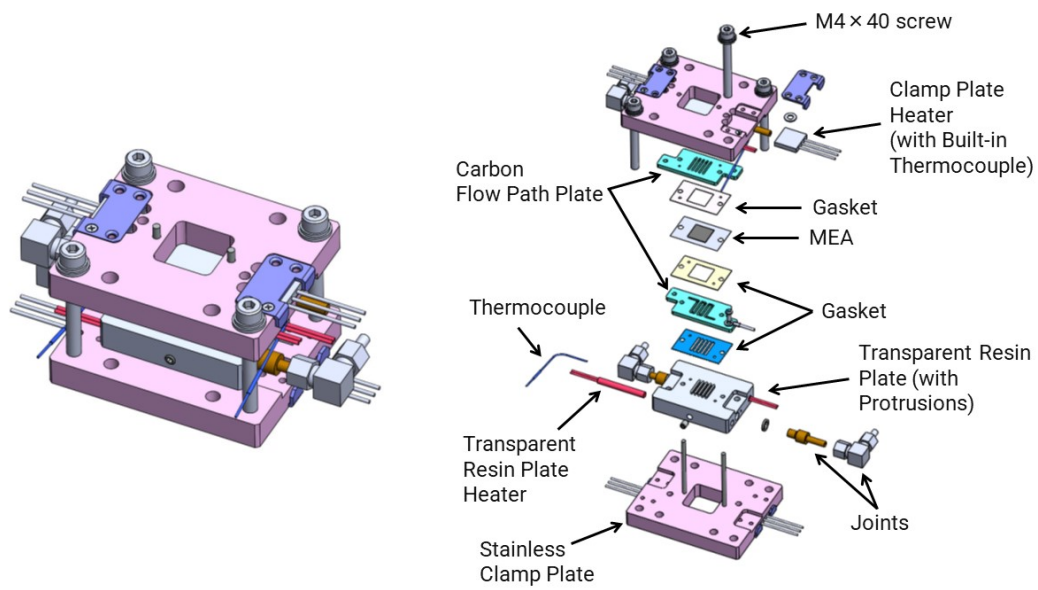


Figure S1.1: Exploded view of the X-ray analysis cell

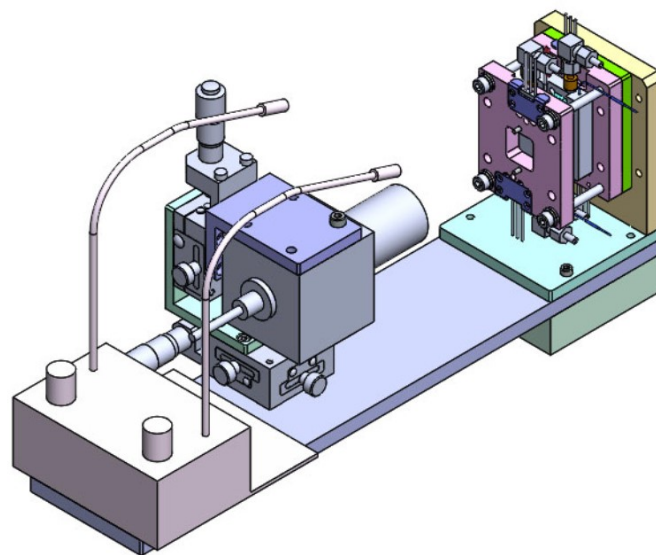


Figure S1.2: Fixture and CMOS visible-light camera configuration

## 1.2 Simplified Experimental Setup for Operando X-ray Imaging

When conducting operando imaging of the X-ray analysis cell at a synchrotron radiation beamline facility, we faced spatial constraints within the hutch where X-rays are irradiated. To address this, we developed a portable simplified experimental setup. Figure S1.3 illustrates this setup, which includes a gas supply, electrolyte circulation equipment (bottles, vials, and a pump), a temperature controller, a DC power supply for driving the X-ray analysis cell, and a gas sensor for gas quantification.

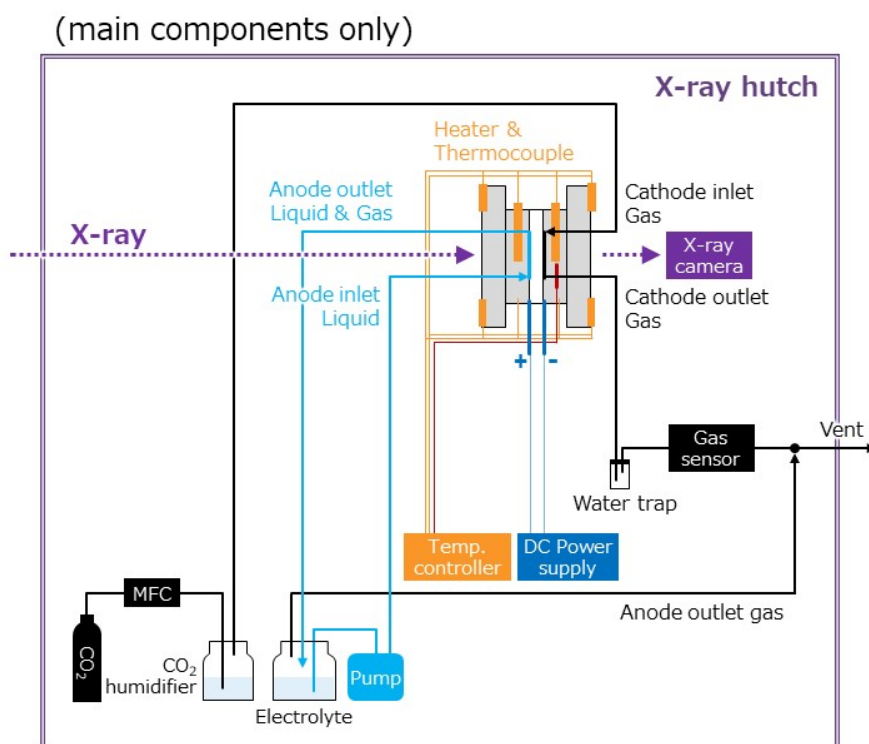


Figure S1.3: Simplified experimental setup

These devices were connected to a PC via a USB hub, allowing real-time monitoring and control during operando operation. The operando protocol involved gradually increasing the current while acquiring X-ray transmission images (Figure S1.4 and Table S1.1).

Flow direction in visible-light and X-ray imaging results are explained in Figure S1.5, using images at 700 mA cm<sup>-2</sup> for example.

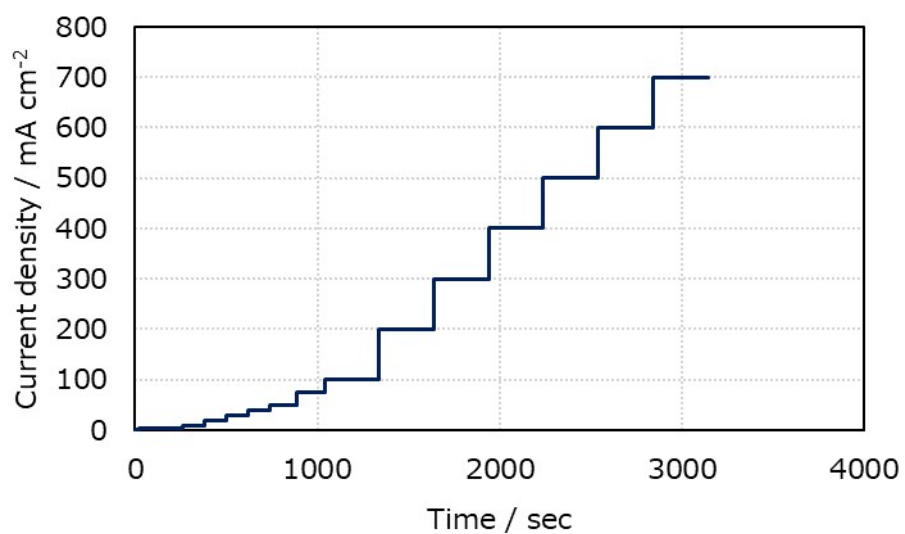


Figure S1.4: Current application protocol

Table S1.1: Detail of the current application protocol

Current density mA/cm <sup>2</sup>	Step duration min	Start time sec	End time sec
0	0.33	t = 0	t = 20
5	4	20	260
10	2	260	380
20	2	380	500
30	2	500	620
40	2	620	740
50	2.5	740	890
75	2.5	890	1040
100	5	1040	1340
200	5	1340	1640
300	5	1640	1940
400	5	1940	2240
500	5	2240	2540
600	5	2540	2840
700	5	t = 2840	t = 3140

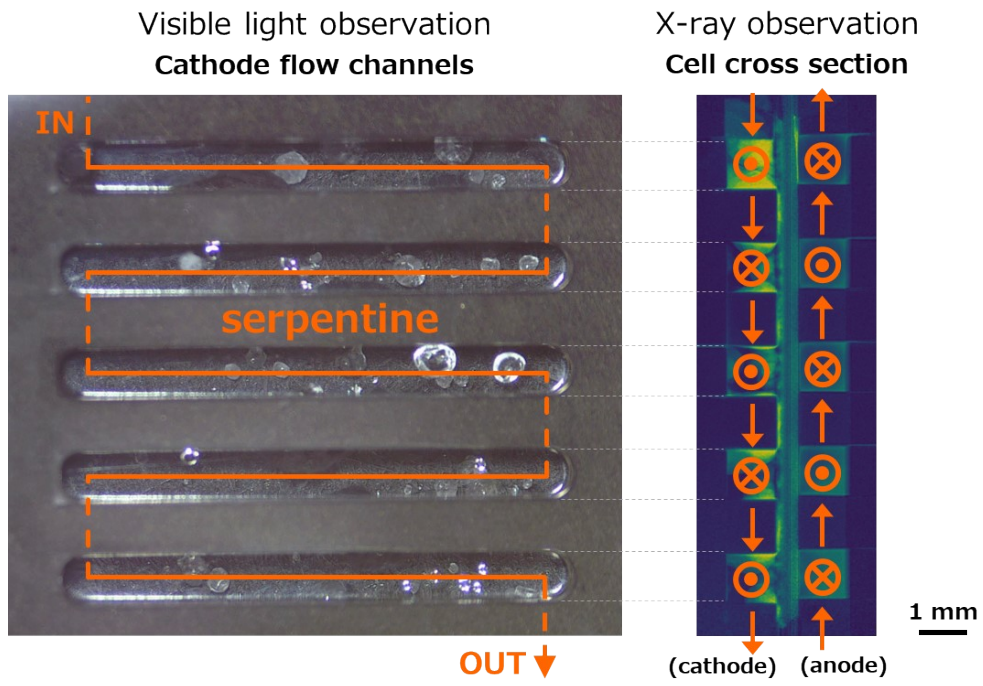


Figure S1.5: Flow direction in imaging results

## 2 Analysis Method for X-ray Imaging Videos

### 2.1 Liquid Thickness and Saturation Derivation

In our X-ray imaging study, we acquired several sets of raw data corresponding to different stages of the experiment. These data were obtained using a CMOS camera specifically designed for X-ray applications (Hamamatsu C12849-101U). Examples of the raw X-ray transmission images are shown in Figure S2.1. The different datasets include the following:

1. **Dark Count ( $I^{\text{raw}}_{\text{dark}}$ ):** This represents the image captured when X-rays are not being irradiated. It serves as a baseline for offset subtraction.
2. **Pre-Operation State ( $I^{\text{raw}}_{\text{empty}}$ ):** Taken just before starting the X-ray analysis cell operation, this dataset captures the initial state without any electrolyte flowing inside the cell.
3. **Operation States ( $I^{\text{raw}}_t$ ):** This dataset represents the X-ray imaging video from immediately after starting the operation ( $t = 0$ ) to the end of the operation. The video was taken at a frame rate of 10 frames per second with a spatial resolution of  $6.5 \mu\text{m}/\text{pixel}$ .

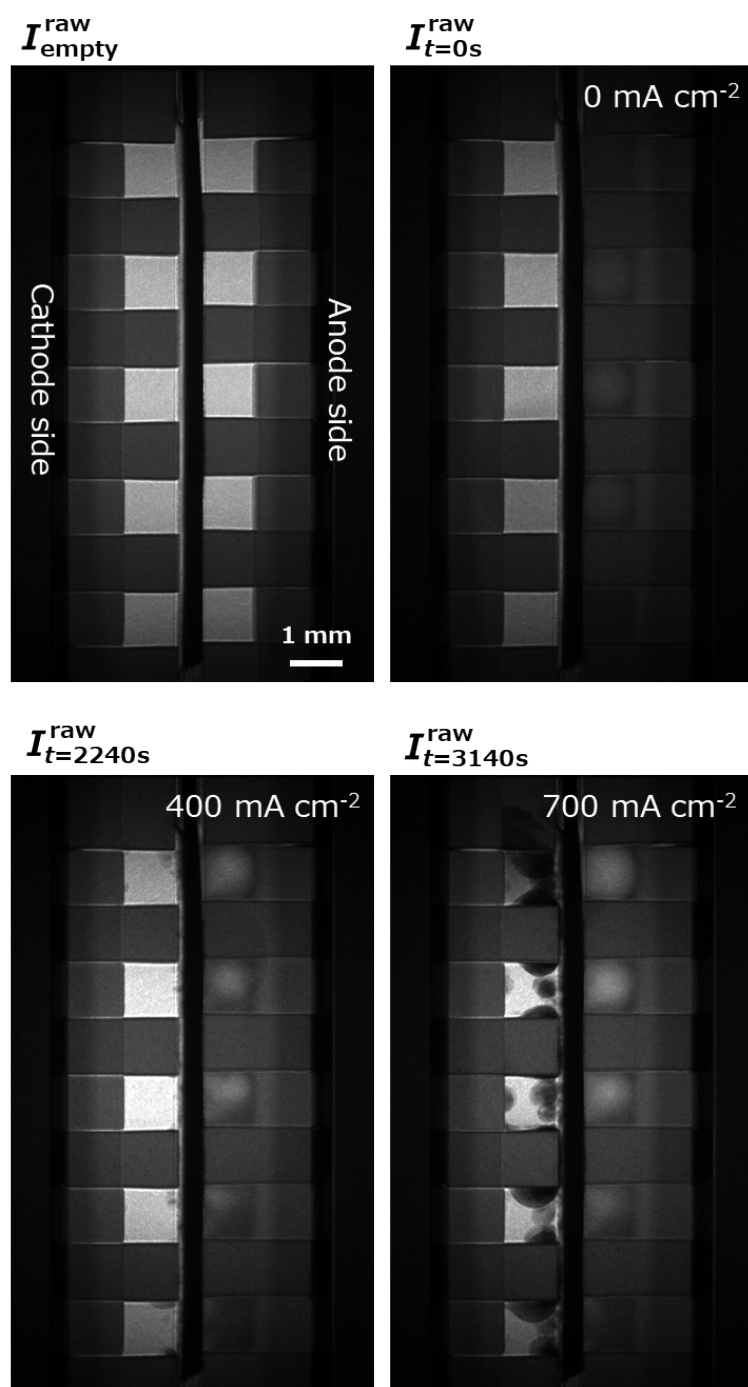


Figure S2.1: Examples of the raw X-ray transmission images

By appropriately analyzing and processing raw X-ray imaging data, we obtained spatial distribution and temporal variations of liquid saturation. We present the details of the analysis below.

Following Lambert-Beer's law, we assumed that the liquid depth at a certain point of the cell viewed from the cross-sectional direction ( $L_{w,t}$ ) is proportional to the natural logarithm of the ratio of incident light intensity ( $I_0$ ) to transmitted light intensity ( $I$ ).

$$L_{w,t} \propto \ln \left( \frac{I_0}{I} \right) \#(S1)$$

Here,  $I_0$  corresponds to the transmitted light intensity from the X-ray analysis cell without electrolyte solution ( $I_{empty}^{raw}$ ), and  $I$  corresponds to the time-varying transmitted light intensity ( $I_t^{raw}$ ) from just after operation initiation to the end of operation.

Considering that the absorptivity and thickness of different components (cathode flow path, cathode, AEM, anode, and anode flow path) within the X-ray analysis cell do not vary with time, we expect any changes in transmitted light intensity to correspond to liquid infiltration in each component. During operation, as liquid accumulates in the cathode, AEM, and anode, the transmitted light intensity decreases due to X-ray absorption by the liquid.

Based on these considerations, we defined the liquid depth ( $L_{w,t}$ ) at a specific time using the following equation, inspired by fuel cell analysis [1]:

$$L_{w,t} = \frac{1}{\mu_w} \ln \left( \frac{I_{empty}^{raw} - I_{dark}^{raw}}{I_t^{raw} - I_{dark}^{raw}} \right) \#(S2)$$

Here,  $1/\mu_w$  represents the X-ray attenuation length for water at 15 keV. According to the above equation, we obtained a separate video composed of pixel values representing  $L_{w,t}$  (32-bit floating-point numbers).

First,  $1/\mu_w = 0.66$  cm was assumed based on the literature data [2]. The resultant liquid depth in the anode flow path just after operation initiation ( $L_{w,0}$ ) was approximately 1.28 cm. Assuming that the anode flow path was initially filled with electrolyte and no gas bubbles,  $L_{w,0}$  should be equal to 1 cm. Thus, we corrected the  $1/\mu_w$  value to 0.516 cm. Differences from literature values may arise from variations in water and electrolyte absorptivity.

Using the corrected absorptivity, we defined the liquid saturation ( $S_{w,t}$ ) at a specific time [1]:

$$S_{w,t} = \frac{L_{w,t}}{z \varepsilon_i} \#(S3)$$

Here,  $z$  represents the depth of the cell components (assumed to be 1 cm), and  $\varepsilon_i$  corresponds to the porosity of each component (values from Table S2.1). We assumed the AEM to be fully saturated ( $\varepsilon = 1$ ).

Table S2.1: Porosity of MEA components

<b>MEA Component</b>	<b>Component Description</b>	<b>Thickness [<math>\mu\text{m}</math>]</b>	<b>Porosity <math>\varepsilon_i</math></b>
<b>Cathode</b>	Gas Diffusion Layer (Sigracet 28BC)	227.5	0.8
	Catalyst Layer	32.5	0.6
<b>Membrane</b>	PiperION	19.5	1 (assumed)
<b>Anode</b>	IrO <sub>x</sub> on Ti Mesh	214.5	0.56

Using the component thicknesses, we generated an image of the spatial distribution of  $\varepsilon_i$  (Figure S2.2). The thicknesses, which was measured from the X-ray transmission images, possibly include errors due to factors such as the deviation in the angle of incidence (the incident X-ray angle was adjusted in  $0.1^\circ$  increments). Dividing the images of  $L_{w,t}$  at each time by the  $\varepsilon_i$  image yielded a video, each pixel value representing  $S_{w,t}$  at that location.

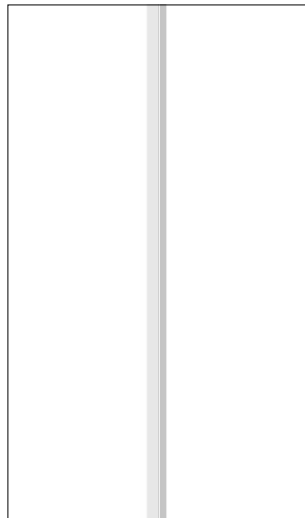


Figure S2.2: Virtual  $\varepsilon_i$  distribution in the MEA

The resulting analysis provided spatial distribution of liquid saturation at different time points. The image processing package Fiji [3] was used for this analysis.

The X-ray absorption by the gas phase was disregarded in this analysis. For X-rays with a transmission length of 1 cm and energy of 15 keV, estimated transmittance values are 22.1% for pure water, 19.8% for 0.1 M  $\text{KHCO}_3$  solution, 10.1% for 1 M  $\text{KHCO}_3$  solution, and 99.7% for  $\text{CO}_2$  gas, as shown in Figure S2.3. Since X-rays are hardly absorbed by  $\text{CO}_2$  gas, the contribution of the gas phase can be ignored.

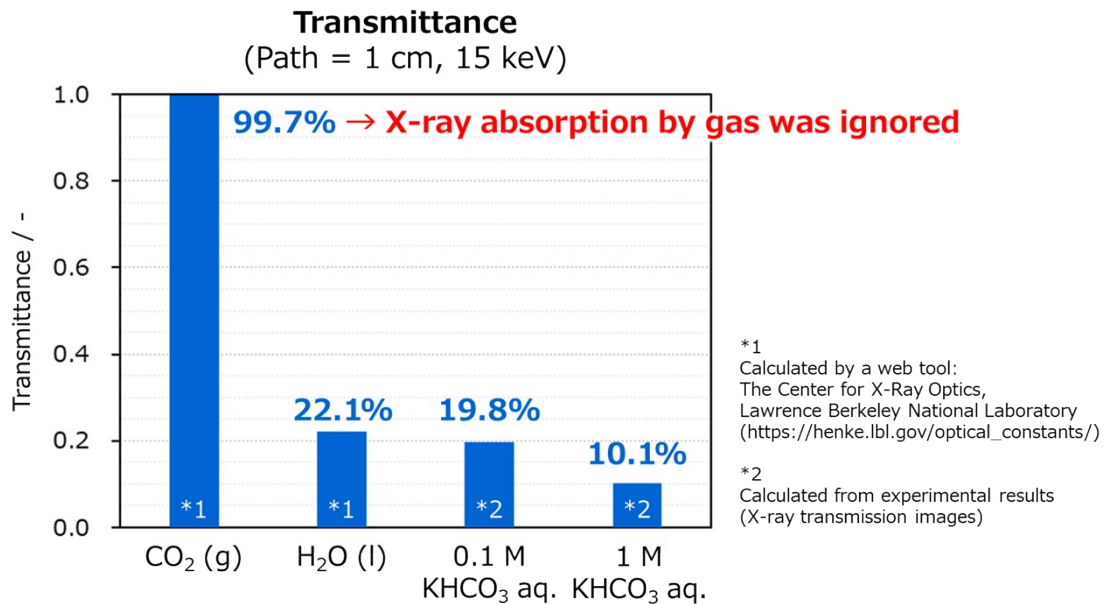


Figure S2.3: Comparison of X-ray transmittance rates for  $\text{CO}_2$  gas, distilled water, and different concentrations of electrolyte solutions

## 2.2 Liquid Flux and Flow Rate

A method to derive liquid flux and flow rate based on the temporal distribution of the absolute liquid content is described below.

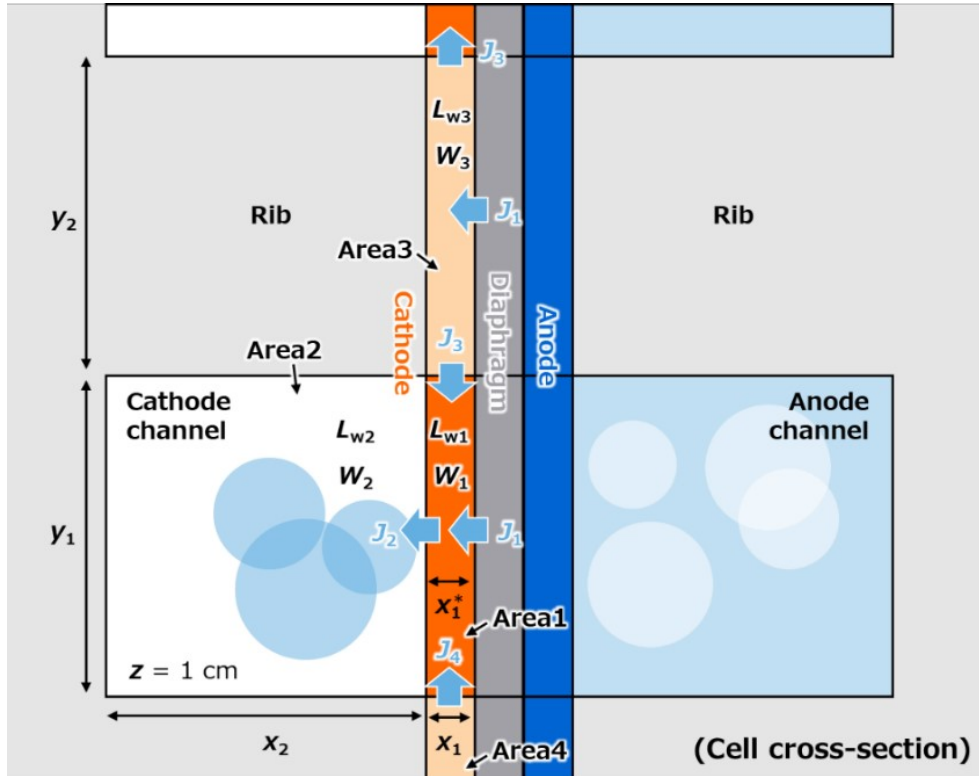


Figure S2.4: Areas 1~4 and liquid fluxes  $J_{1,r} \sim J_{4,t}$  considered in the present analysis

Figure S2.4 is the schematic diagram of the cell cross-section, illustrating the phenomena considered in the present analysis. Although the diagram depicts a vertically oriented MEA, the same principles apply even if the MEA were horizontally oriented.

We focused on a specific cathode portion (referred to as Area 1), which includes the cathode catalyst layer, microporous layer, and gas diffusion layer. The adjacent cathode channel is labeled as Area 2, and the cathode portions adjacent to the upper and lower ribs are Areas 3 and 4, respectively.

The labeled dimensions for each area are provided in Table S2.2, with a common depth (in the  $z$  direction, according to the conventions of Figure S2.4) of 1 cm.

For each area (1~4), we defined the average liquid depth as  $\bar{L}_{wn,t}$  (where  $n = 1, 2, 3, 4$ ). The total change in liquid amount within each area over time ( $W_{n,t}$ ) was expressed by the following equations:

$$W_{1,t} = x_1^* y_1 \frac{\Delta \bar{L}_{w1,t}}{\Delta t} \#(S4)$$

$$W_{2,t} = x_2 y_1 \frac{\Delta \bar{L}_{w2,t}}{\Delta t} \#(S5)$$

$$W_{3,t} = x_1 y_2 \frac{\Delta \bar{L}_{w3,t}}{\Delta t} \#(S6)$$

$$W_{4,t} = x_1 y_2 \frac{\Delta \bar{L}_{w4,t}}{\Delta t} \#(S7)$$

The measurement data were obtained every second, so the time dependent term  $\Delta \bar{L}_{wn,t}/\Delta t$  in above equations was calculated by taking the difference between the data one second before and one second after a certain time.

Table S2.2: Labeled dimensions for each area

Area No.	Width	Height	Depth
1	$x_1^*$	$y_1$	$z$
2	$x_2$	$y_1$	$z$
3	$x_1$	$y_2$	$z$
4	$x_1$	$y_2$	$z$

In our calculations, we considered the following assumptions related to liquid movement within the cell:

1. In the cathode portion adjacent to the cathode flow channel (Area 1) and the cathode portions adjacent to the ribs (Areas 3 and 4), the liquid flux entering from the membrane at a given time is equal, and is labeled as  $J_{1,t}$ .
2. From Area 3, the liquid flows evenly into the cathode portions that interface with the upper and lower ribs (with the lower side corresponding to Area 1) with a flux of  $J_{3,t}$ . Similarly, from Area 4, the liquid moves evenly into the cathode portions that interface with the upper and lower ribs (with the upper side corresponding to Area 1) with a flux of  $J_{4,t}$ . It is necessary to formulate the one-sided movement for the upper and lower ends where adjacent flow paths or ribs do not exist.

3. Liquid enters Area 2 exclusively from Area 1 with a flux of  $J_{2,t}$ .
4. No liquid exits from Area 2. In other words, the liquid does not cross over the serpentine fold and is not discharged outside the cell.

Assumption #1 implies that the cathode area's state remains the same in the portions adjacent to the flow channel and those adjacent to the rib. However, in practical electrochemical cells, variations in current density, temperature, and material diffusion are possible. Such variations are difficult to measure directly, so simulations or other means will be needed to verify the validity of Assumption #1. Assumption #2 disregards the influence of gravity. The magnitude of gravity's impact, which is thought to be minor, could potentially be evaluated by comparing the performance of MEAs in vertical and horizontal configurations. Assumption #4 is valid under the current test conditions because it was found in the through-plane visible-light observation with a CMOS camera that the droplets seeped out into the cathode flow channels remained at the same place during the experiment.

Under the assumptions #1~#4 mentioned above, we analyze the mass balance in each area. Considering that the difference between inflowing and outflowing liquid equals the liquid accumulation within each area, the following relationships hold:

$$y_1z * J_{1,t} + x_1z * J_{3,t} + x_1z * J_{4,t} = W_{1,t} + y_1z * J_{2,t} \#(S8)$$

$$y_1z * J_{2,t} = W_{2,t} \#(S9)$$

$$y_2z * J_{1,t} = W_{3,t} + 2x_1z * J_{3,t} \#(S10)$$

$$y_2z * J_{1,t} = W_{4,t} + 2x_1z * J_{4,t} \#(S11)$$

By solving above equations simultaneously for  $J_{1,t} \sim J_{4,t}$ , we can calculate the liquid flux within the cell at each point in time.

$$J_{1,t} = \frac{2W_{1,t} + 2W_{2,t} + W_{3,t} + W_{4,t}}{2(y_1 + y_2)z} \#(S12)$$

$$J_{2,t} = \frac{W_{2,t}}{y_1z} \#(S13)$$

$$J_{3,t} = \frac{2y_2W_{1,t} + 2y_2W_{2,t} - (2y_1 + y_2)W_{3,t} + y_2W_{4,t}}{4x_1(y_1 + y_2)z} \#(S14)$$

$$J_{4,t} = \frac{2y_2W_{1,t} + 2y_2W_{2,t} + y_2W_{3,t} - (2y_1 + y_2)W_{4,t}}{4x_1(y_1 + y_2)z} \#(S15)$$

Focusing on Area 1, we define flow rates  $Q_{1,t} \sim Q_{4,t}$  as shown in Figure 3c in the main text, by multiplying the fluxes  $J_{1,t} \sim J_{4,t}$  by their respective areas (e.g.,  $Q_{1,t} = J_{1,t} * y_1z$ ). The flow rate values obtained every second were highly variable, so they were averaged every

minute (every 1.25 minutes for current densities of 50 and 75 mA cm<sup>-2</sup>, dividing the holding time of 2.5 minutes into two) and graphed (Figure 3d in the main text).

It should be noted that the evaporation of liquid water was not considered in the calculation above. The following shows an example of how equations can be modified when taking the evaporation into account. Here we consider two evaporation phenomena (Figure S2.5): One is the evaporation of liquid water in Area 1. The resultant steam is considered to diffuse into the adjacent gas phase in Area 2. The other is the evaporation of liquid water in Area 2 (droplets generated in the cathode flow channel), where steam is also considered to diffuse into the gas phase in Area 2. Assuming that the evaporation rate corresponding to the first phenomenon is  $kQ_{evap}$ , and that corresponding to the second phenomenon is  $(1-k)Q_{evap}$ , Equations S8~11 can be modified as follows:

$$y_1z * J_{1,t} + x_1z * J_{3,t} + x_1z * J_{4,t} = W_{1,t} + y_1z * J_{2,t} + kQ_{evap} \#(S16)$$

$$y_1z * J_{2,t} = W_{2,t} + (1 - k)Q_{evap} \#(S17)$$

$$y_2z * J_{1,t} = W_{3,t} + 2x_1z * J_{3,t} \#(S18)$$

$$y_2z * J_{1,t} = W_{4,t} + 2x_1z * J_{4,t} \#(S19)$$

Therefore, liquid fluxes  $J_{1,t} \sim J_{4,t}$  will be obtained as follows:

$$J_{1,t} = \frac{2W_{1,t} + 2W_{2,t} + W_{3,t} + W_{4,t} + 2Q_{evap}}{2(y_1 + y_2)z} \#(S20)$$

$$J_{2,t} = \frac{W_{2,t} + (1 - k)Q_{evap}}{y_1z} \#(S21)$$

$$J_{3,t} = \frac{2y_2W_{1,t} + 2y_2W_{2,t} - (2y_1 + y_2)W_{3,t} + y_2W_{4,t} + 2y_2Q_{evap}}{4x_1(y_1 + y_2)z} \#(S22)$$

$$J_{4,t} = \frac{2y_2W_{1,t} + 2y_2W_{2,t} + y_2W_{3,t} - (2y_1 + y_2)W_{4,t} + 2y_2Q_{evap}}{4x_1(y_1 + y_2)z} \#(S23)$$

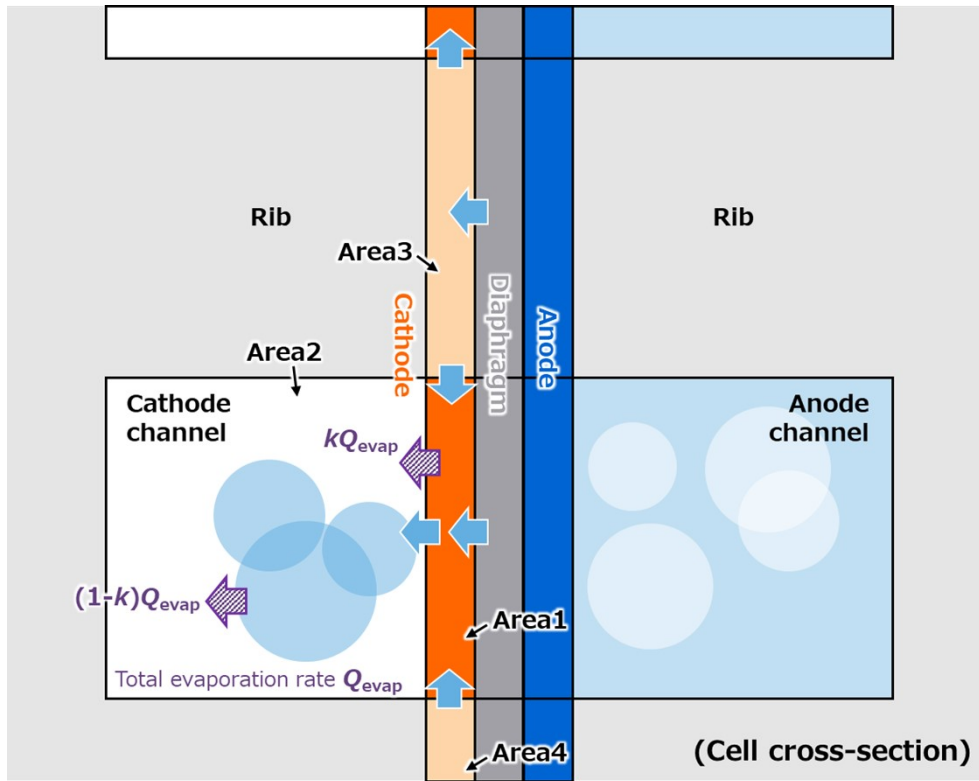


Figure S2.5: Water evaporation phenomena

### 3 Preliminary Experiment: CO<sub>2</sub> Electrolysis Performance of the Imaging Cell

#### 3.1 Experimental

Preliminary CO<sub>2</sub> electrolysis test was conducted using the X-ray imaging cell. The anode, the cathode, and the membrane were the same as those used in the operando X-ray imaging experiment. The apparatus for the preliminary test is illustrated in Figure S3.1. The gas exiting the cathode is diluted with argon (Ar) and introduced into the line of a gas chromatograph (Micro GC Fusion, Inficon) or a flow meter. Heaters are provided to heat the cathode inlet and anode inlet pipes. The pipe temperature was set at 40°C. No heating was performed on the cell. The CO<sub>2</sub> flow rate was set at 20 sccm, and the dilution Ar flow rate was set at 380 sccm. The flow rate of the anode electrolyte solution (0.1 M KHCO<sub>3</sub> aq.) was set at 5 mL min<sup>-1</sup>. The current density was increased every 10 minutes to 10, 50, 100, 300, 500, 700, 1000 mA cm<sup>-2</sup>, and the gas flow rate and gas composition at the cathode outlet after dilution were analyzed and recorded at each step.

Cathode Faraday efficiency ( $\eta_k$ ,  $k = \text{CO}$  or  $\text{H}_2$ ) was calculated by the following formula:

$$\eta_k = \frac{2n_k F}{iA} \quad \#(S24)$$

where  $n_k$  is the molar flow rate of species  $k$  at the cathode outlet,  $F$  is the Faraday constant,  $i$  is the current density, and  $A$  is the electrode area (1 cm<sup>2</sup>).

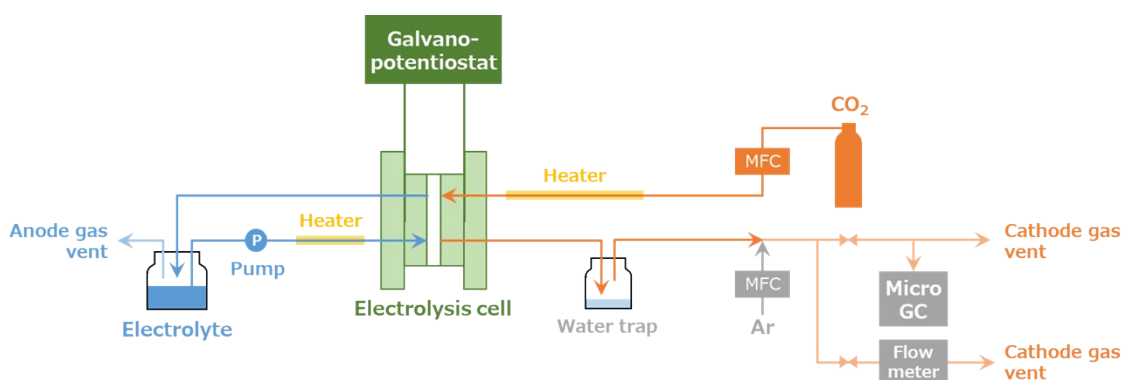


Figure S3.1: Experimental apparatus for preliminary CO<sub>2</sub> electrolysis test

#### 3.2 Results

Figure S3.2(a) shows the current density and the cell voltage recorded in the preliminary experiment. The cell voltage was stable in each step with current density up

to  $400 \text{ mA cm}^{-2}$  but increased with time with the current density of  $500 \text{ mA cm}^{-2}$  and larger. This implies that the cathode flooding proceeded with time at high current densities. Figure S3.2(b) shows the cathode Faraday efficiency (FE). The CO FE reached its maximum (*ca.* 90%) at  $200 \text{ mA cm}^{-2}$  and decreased gradually. The  $\text{H}_2$  FE increased at the same time and the total FE remained constant. Table S3.1 shows the calculated  $\text{CO}_2$ -to-CO conversion ratio at each current density, incorporating mass balance that accounts for crossover effects. Note that even with crossover, the  $\text{CO}_2$ -to-CO conversion ratio remains below 20%, suggesting that local environment around the catalyst remains sufficiently rich in  $\text{CO}_2$  to maintain stable reaction conditions.

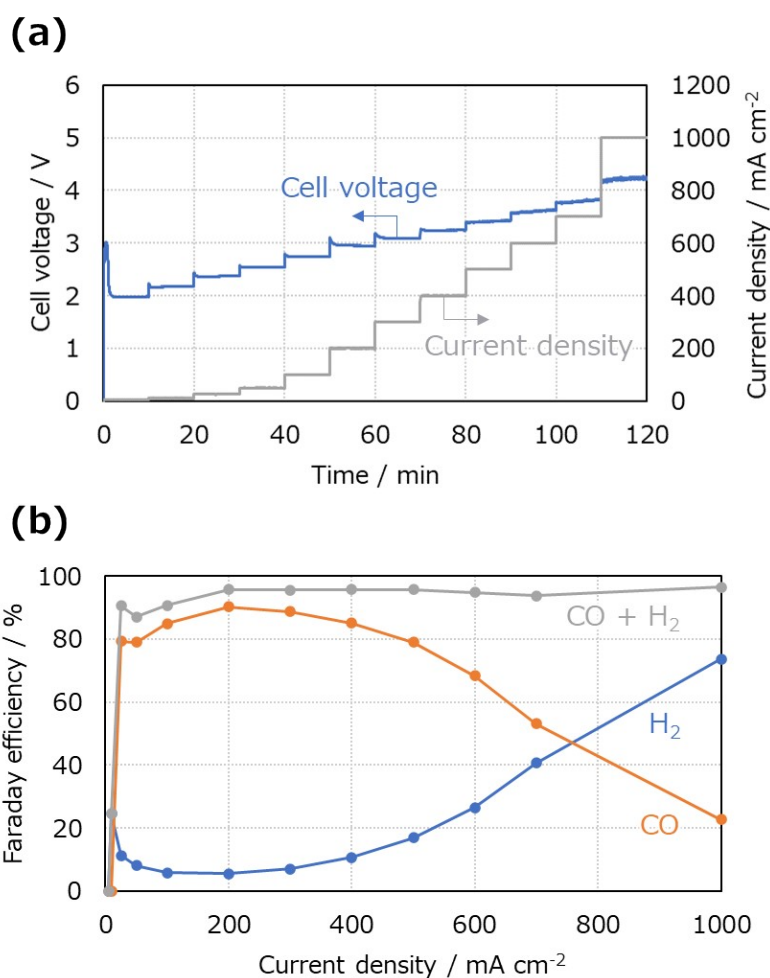


Figure S3.2: CO<sub>2</sub> Electrolysis performance of the imaging cell  
(a) Cell voltage (b) Cathode Faraday efficiency

Table S3.1: Calculated CO<sub>2</sub>-to-CO conversion ratio at each current density

Current density	CO <sub>2</sub> -to-CO conversion ratio
mA/cm <sup>2</sup>	%
25	0.7
50	1.4
100	3.0
200	6.3
300	9.3
400	11.9
500	13.8
600	14.3
700	13.0
1000	7.4

## References

1. Guan, R., Bazylak, A. Resolving mass transport losses at the catalyst layer of polymer electrolyte membrane fuel cells through semi-empirical modelling. *Electrochimica Acta* 447, 142103 (2023).  
<https://doi.org/10.1016/j.electacta.2023.142103>.
2. Lawrence Berkeley National Laboratory (Berkeley Lab), The Center for X-ray Optics “X-Ray Interactions With Matter / Filter Transmission”  
([https://henke.lbl.gov/optical\\_constants/filter2.html](https://henke.lbl.gov/optical_constants/filter2.html))
3. Fiji (<https://imagej.net/software/fiji/>)